Science of the Total Environment 584–585 (2017) 381–392

Contents lists available at ScienceDirect

Science of the Total Environment

journal homepage: www.elsevier.com/locate/scitotenv

Regional transport of anthropogenic pollution and dust aerosols in spring to Tianjin — A coastal megacity in China

Xiaoli Su [a,b], Qiao Wang [c], Zhengqiang Li [d], Mariarosaria Calvello [e], Francesco Esposito [f], Giulia Pavese [e], Meijing Lin [g], Junji Cao [a,b,*], Chunyan Zhou [c], Donghui Li [d], Hua Xu [d]

[a] Key Lab of Aerosol Chemistry & Physics, Chinese Academy of Sciences (KLACP), Chinese Academy of Sciences, Xi'an 710061, China
[b] SKLLQG, Institute of Earth Environment, Chinese Academy of Sciences, Xi'an 710061, China
[c] State Environmental Protection Key Laboratory of Satellite Remote Sensing, Satellite Environment Center, Ministry of Environmental Protection of the People's Republic of China, Beijing 100094, China
[d] Institute of Remote Sensing and Digital Earth, Chinese Academy of Sciences, Beijing 100101, China
[e] Istituto di Metodologie per l'Analisi Ambientale - CNR, Tito Scalo 85050, Italy
[f] Scuola di Ingegneria-Università della Basilicata, Potenza 85100, Italy
[g] Zhongshan Bureau of Meteorology, Zhongshan 528400, China

HIGHLIGHTS

- Simultaneous measurements of aerosol optical properties and PM2.5 chemical compositions were investigated in Tianjin, China.
- Two typical types of pollution episodes were identified in spring over the coastal megacity.
- Regional transports of both anthropogenic pollution and dust aerosols contributed to the spring haze in Tianjin.

GRAPHICAL ABSTRACT

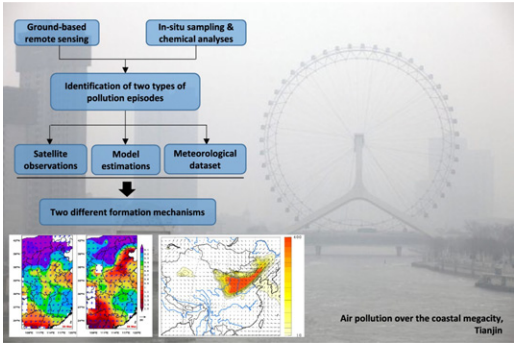

ARTICLE INFO

Article history:
Received 28 September 2016
Received in revised form 14 December 2016
Accepted 3 January 2017
Available online 31 January 2017

Editor: D. Barcelo

Keywords:
Multi-scale observations
Urban pollution
Dust transport
Formation mechanism

ABSTRACT

Simultaneous measurements of columnar aerosol microphysical and optical properties, as well as $PM_{2.5}$ chemical compositions, were made during two types of spring pollution episodes in Tianjin, a coastal megacity of China. The events were investigated using field observations, satellite data, model simulations, and meteorological fields. The lower Ångström Exponent and the higher aerosol optical depth on 29 March, compared with the earlier event on 26 March, implied a dominance of coarse mode particles — this was consistent with the differences in volume-size distributions. Based on the single scattering spectra, the dominant absorber (at blue wavelength) changed from black carbon during less polluted days to brown carbon on 26 March and dust on 29 March. The concentrations of major $PM_{2.5}$ species for these two episodes also differed, with the earlier event enriched in pollution-derived substances and the later with mineral dust elements. The formation mechanisms of these two pollution episodes were also examined. The 26 March episode was attributed to the accumulation of both local emissions and anthropogenic pollutants transported from the southwest of Tianjin under the control of high pressure system. While the high aerosol loading on 29 March was caused by the mixing of transported dust from northwest source region with local urban pollution. The mixing of transported anthropogenic pollutants

* Corresponding author at: Key Lab of Aerosol Chemistry & Physics, Chinese Academy of Sciences (KLACP), Chinese Academy of Sciences, Xi'an 710061, China.
E-mail address: cao@loess.llqg.ac.cn (J. Cao).

http://dx.doi.org/10.1016/j.scitotenv.2017.01.016

and dust with local emissions demonstrated the complexity of springtime pollution in Tianjin. The synergy of multi-scale observations showed excellent potential for air pollution study.

1. Introduction

Rapid industrialization and urbanization have led to an increase in air pollution at local to global scales over the last two centuries. The types and concentrations of air pollutants have also undergone drastic changes as technology and manufacturing have developed and advanced (Fenger, 2009). In China, aerosol particles (also called particulate matter or PM) have caused severe environmental problems and attracted increasing interest in recent years (Huang et al., 2014). This is particularly the case in megacity clusters, such as the Beijing-Tianjin-Hebei Province (BTH) area in the North China Plain (NCP); the Pearl River Delta (PRD); and the Yangtze River Delta (YRD) regions (Tie and Cao, 2009). Due to the heavy oil and coal consumption need to support the economic, high aerosol loading have occurred in these densely populated regions (Zhao et al., 2013a; Mao et al., 2014; Zhang et al., 2012), and the particles have affected human health, visibility, ecological health and climate change (Kaufman et al., 2002; Pöschl, 2005; Cao et al., 2012a, b; Wang et al., 2013a; Tie et al., 2016).

The BTH region is one of the most important economic and population centers in China, accounting for 10.4% of the national Gross Domestic Product (GDP) and 16.2% of the national population in 2014 (http://www.stats.gov.cn/). The BTH is also one of the areas most strongly affected by haze pollution in China, if not the world: the visibility there has decreased regularly from 1980 to 2008, and the number of hazy days has increased since the 1990s (Zhao et al., 2011). Numerous studies have been conducted in this region to characterize aerosol pollution and investigate the formation mechanism of haze events, (He et al., 2009; Quan et al., 2011; Zhao et al., 2013b, c; Zhang et al., 2013; Liu et al., 2013; Wang et al., 2016), especially since January 2013 when an historic severe fog-haze event occurred over central and eastern China (Guo et al., 2014; Wang et al., 2014a; Tao et al., 2014). That severe haze event was attributed to the rapid conversion of gaseous precursor to secondary aerosols under stagnant meteorological conditions (Zhang et al., 2014a) in Wang et al. (2014b). A study by Zhang et al. (2014b) also highlighted the contribution of regional transport to that pollution episode through the analysis of data from chemical analyses. Using both trajectory-cluster and receptor models, Wang et al. (2015) showed that long-distance transportation contributed 35.5% of the $PM_{2.5}$ in Beijing from 2005 to 2010. This was comparable to the contribution of 26% to 35% from transport for cities inside the BTH reported by Wang et al. (2014c). Despite the considerable amount of researches on BTH haze episodes, the mechanism responsible for the aerosol pollution remained unclear (Hu et al., 2015). Specifically, with regard to the regions outside Beijing, such as Tianjin and Hebei Province, even the microphysical and optical properties as well as chemical characteristics of haze aerosol are not well characterized. Furthermore, previous studies have mostly focused on wintertime haze events, and they have rarely investigated pollution episodes in spring. The spring and winter events are both characterized by low visibility and high PM concentrations, but those in spring are complicated by the mixing of mineral dust with local anthropogenic aerosols (Yuan et al., 2008; Tie and Cao, 2009).

For the present study, simultaneous investigations of aerosol microphysical and optical properties were conducted at three sites in Tianjin during March 2012. Two types of high aerosol loading were identified, and we used a combination of in-situ measurements, satellite observations, model simulations, and meteorological analyses to explore the factors that led to the pollution episodes. Moreover, a technique was developed and applied to assess the contribution of different aerosol components to the total aerosol extinction, and this provided insights into the different causes for pollution events. The objectives of this study were to identify the main factors responsible for urban pollution at a coastal megacity; these results may lead to improvements in environmental policies in China.

2. Instrumentation and methodology

2.1. Site description

Tianjin is one of the largest municipalities in China, having a population of ~15 million and covering an area of 11,919 km^2. It is located to the southeast of Beijing and adjacent to the Bohai Sea. As an important industrial center and a well-developed economic hub, Tianjin has experienced increasing aerosol pollution in recent years (Ji et al., 2012), but the studies on air quality have been rather limited. According to Zhao et al. (2011), the averaged visibility in Tianjin from 1980 to 2008 was only 13.6 km, and that is considerably less than in Beijing (21.7 km). Moreover, Tianjin has experienced a continuous decreasing trend in visibility beginning 2005 (Chen and Xie, 2014). Fugitive dust, motor vehicle exhaust, industrial emissions, and biomass burning all pollute the air, and PM is the principal pollutant in the region (Bi et al., 2007).

In this study, three sites were chosen in urban, industrial and coastal areas of Tianjin, and aerosol microphysical and optical properties were simultaneously measured at these sites along with the chemical characteristics of fine PM. As shown in Fig. 1, the Hexi site was located downtown in the Hexi district (orange area in Fig. 1), ~55 m from the urban ring expressway and surrounded by residences, restaurants, shops and heavy traffic. The industrial site was situated in the Dongli district (marked in blue) where there were numerous small- and medium-sized factories nearby; these include machinery, chemical manufacturing plants, automotive fitting factories, and electronics facilities. The third site was located in Tanggu district (green portion in Fig. 1), and it was contiguous with the Tianjin Economic-technological Development Area where there were 271 industrial enterprises that accounted for >100 million yuan of total industrial production value in 2012. Several coal-fired power plants and gas stations, along with these industries near Tanggu, consumed large quantities of energy and that has resulted in high pollution emissions in the region (Kong et al., 2010). In this paper, the Hexi, Dongli and Tanggu sites were abbreviated as HX, DL and TG, respectively.

2.2. Instrumentation and datasets

2.2.1. Ground-based columnar aerosol physical properties

Columnar aerosol microphysical and optical properties were simultaneously retrieved from observations made with CIMEL CE-318 sun-sky radiometer (*Cimel Electronique, Paris, France*) deployed at each of the three sites. The automatic radiometer use eight wavelengths for aerosol observations, nominally centered at 340, 380, 440, 500, 675, 870, 1020 and 1640 nm with bandwidth from 2 to 10 nm. In addition, it also worked at 940 nm, which was used to derive the column-integrated water vapor (WV, in cm). Measurements of direct solar irradiance were automatically scheduled every 15 min and the variability of those measurements was used to detect clouds (Smirnov et al., 2000). The comprehensive aerosol retrieval code developed by Dubovik et al. (2000, 2006) was used for data processing. Based on the direct sun measurements, aerosol optical depth (AOD) was retrieved at each nominal wavelength, and the AODs at 440 and 870 nm were used to calculate the Ångström Exponent (AE) (Holben et al., 1998; Dubovik et al., 2000). Sky radiance scanned in almucantar and solar principal plane were used to retrieve aerosol microphysical properties, including size

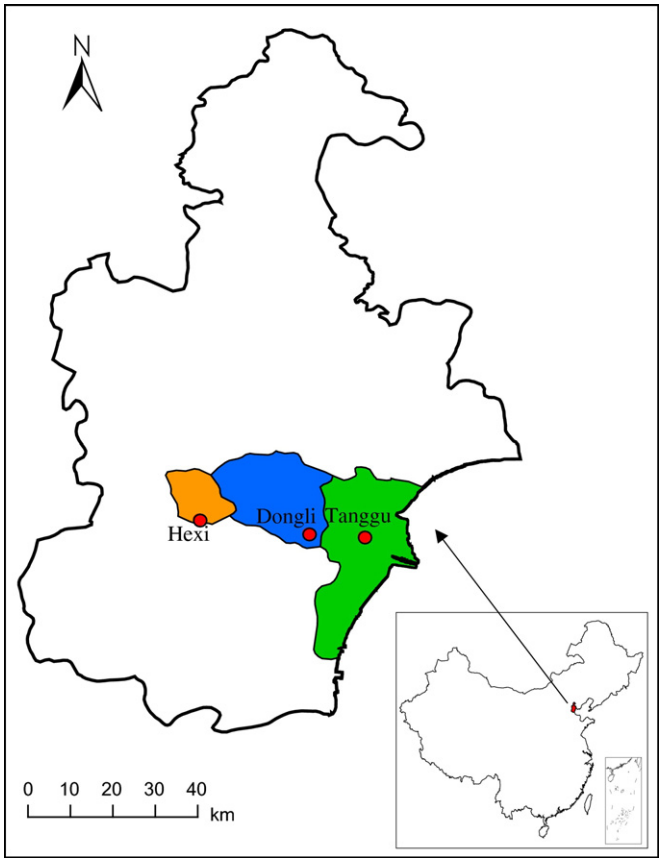

Fig. 1. Locations of the Hexi (HX, urban), Dongli (DL, industrial) and Tanggu (TG, coastal) sites in Tianjin.

distribution (typical uncertainty of 25%), complex refractive index (typical uncertainty of ±0.04 for real parts and 40% for imaginary parts), and single scattering albedo (SSA, typical uncertainty of ±0.03), together with direct solar measurements at 440, 675, 870, and 1020 nm (Dubovik et al., 2000, 2006; Dubovik and King, 2000; Li et al., 2009). The calibration of the instrument and derivation of AOD have been described in detail in Holben et al. (1998) and Li et al. (2008). The accuracy in AOD retrievals from the above algorithms was about 0.01–0.02 (Dubovik et al., 2000).

The main columnar aerosol optical and microphysical data used in this paper were the AODs, AE and volume size distribution (from 0.05 to 15 μm). To match the aerosol physical properties with $PM_{2.5}$ chemical compositions, we used Mie theory to calculate the fine mode AOD (FAOD) for a cut-off radius of 1.0 μm as this corresponded to an aerodynamic diameter of 2.5 μm (Zhang and Li, 2015). The fine mode fraction (FMF) was also computed as the ratio of FAOD to the total AOD (TAOD). Finally, to investigate the characteristics of absorbing particles, the absorption aerosol optical depth (AAOD) was calculated as AOD × (1 − SSA).

2.2.2. Samples collection and chemical analyses

Aerosol fine particle samples ($PM_{2.5}$, particulate matter with aerodynamic diameter ≤ 2.5 μm) were simultaneously collected on both prefired (900 °C, 3 h) 47 mm Whatman QM-A quartz-fiber filters and Teflon™ filters (*Whatman Ltd., Maidstone, England*). Samples were collected every 12 h during daytime (8:00 to 20:00 local time) at three sites from 24 to 30 March 2012. The quartz-filters were used for the analyses of the carbonaceous species and water-soluble inorganic ions while the Teflon™ filters were used for the element analyses.

Chemical analyses of the $PM_{2.5}$ samples were conducted at the Institute of Earth Environment, Chinese Academy of Sciences in Xi'an, China. Water-soluble ions were determined by ion chromatography (Chow and Watson, 1999) (*IC, Dionex 600, Dionex Corp, Sunnyvale, CA*) using one-fourth of each quartz filter sample for the analyses. Detailed pretreatment and analytical procedures were described in Shen et al. (2008) and Zhang et al. (2011). The method detection limits (MDLs) were 4.0, 15.0, 20.0, 8.7 and 1.1 μg L^{-1} for NH_4^+, NO_3^-, SO_4^{2-}, Cl^- and K^+, respectively (Zhang et al., 2014c). The concentrations of carbonaceous species (organic carbon and element carbon, OC and EC, respectively) were determined on a 0.526 cm^2 punch from each quartz sample filter with the use of a DRI (Model 2001) Carbon Analyzer (*Atmoslytic Inc., Calabasas, CA, USA*) following a thermal optical reflectance (TOR) protocol (Chow and Watson, 2002). To determine the concentrations of elemental components, the Teflon™ filter samples were analyzed directly without any preparation procedures using an Energy Dispersive X-ray Fluorescence (ED-XRF) instrument (*Epsilon 5, PANalytical B. V., The Netherlands*) (Watson et al., 1999). Quality assurance/quality control (QA/QC) procedures of the XRF analysis have been described in Xu et al. (2012), and more detailed descriptions of the QA/QC procedures for the other methods may be found in Cao et al. (2003).

To clearly investigate the chemical variations of $PM_{2.5}$ species, we calculated the concentrations of soil dust as the sum of the oxides of Al, Si, Ca, Mg and Ti (i.e., soil dust = 1.89Al + 2.14Si + 1.4Ca + 1.43Fe + 1.66 Mg + 1.67Ti) based on measurements of these elements in mineral dust (Zhao et al., 2007). Organic matter (OM) was also estimated by multiplying the OC concentration by 1.6 (Cao et al., 2003) in this study.

2.2.3. Satellite observations, model simulations and meteorological datasets

As a complement to ground measurements, satellite observations have provided valuable insights into regional air pollution (Chu et al., 2003). The Moderate Resolution Imaging Spectroradiometer (MODIS, King et al., 1992) aboard Terra and Aqua satellite has retrieved comprehensive aerosol datasets from spectral reflectance at 36 bands (0.4 to 14.4 μm) with a swath width of ~2330 km, and it provides global coverage in one or two days. In this study, we used the MODIS Collection 6 AOD products with a spatial resolution of 3 km (Levy et al., 2013) to capture regional characteristics of air pollution events. Additionally, vertical detections from Cloud-Aerosol Lidar with Orthogonal Polarization (CALIOP) aboard the Cloud-Aerosol Lidar and Infrared Pathfinder Satellite Observation (CALIPSO) satellite (CALIPSO V3.02, Omar et al., 2009) were used to help understand the causes for regional pollution.

In addition to the ground-based and satellite observations, simulation results from an operational Chemical weather FORecasting System (RIAM-CFORS) were used when the satellite aerosol retrievals were not available due to cloud contamination. This system integrated a 3-dimensional on-line, regional-scale, chemical transport model fully coupled with the Regional Atmospheric Modeling System, and it has widely used to study regional transport of air pollutant and especially dust transport (Uno et al., 2004; Miura et al., 2014). A detailed description of this system may be found in Uno et al. (2003) and on the website: http://www-cfors.nies.go.jp/~cfors/outline.html. In addition, wind vectors from the European Centre for Medium-Range Weather Forecasts reanalysis datasets (ERA-interim) on 0.125 × 0.125 degree grids (http://www.ecmwf.int/) and surface weather patterns from Korea Meteorological Administration (KMA) were also used to examine the roles of meteorological conditions in the aerosol pollution episodes.

2.3. Radiometric model

To identify the dominant sources of the aerosol pollutants, the technique of Satheesh and Srinivasan (2005) has been improved and applied to evaluate the main components contributing to the columnar AOD (Pavese et al., 2015). Following the approach of Hess et al. (1998), the atmospheric aerosol was assumed to be composed of a variety of components characterized by different size distributions and

refractive indices. The components defined by Hess et al. (1998) were considered in the present study; there were (1) water soluble ions (*WS*); (2) soot (*BC*); (3) accumulation mode sea salt (*SSacc*); (4) coarse mode sea salt (*SScoa*); (5) transported mineral matter (*MT*); (6) nucleation mode mineral matter (*Mnucl*); (7) accumulation mode mineral matter (*Macc*); (8) coarse mode mineral matter (*Mcoa*), and (9) other insoluble materials (*Ins*). Each aerosol component was assumed to have a log-normal size distribution with a fixed mean radius and mode width, as well as characteristic refractive indices (Hess et al., 1998).

The AODs were calculated using the Mie theory from the specific physical and optical parameters mentioned-above.

$$\tau_{\lambda i}^{cal} = \tau_i^{cal} = \sum_{j=1}^{k} \int_0^{\infty} \pi r^2 Q_{extj}(m_j, r, \lambda_j) S_j n_j(r) dr, \quad (1)$$

where Q_{extj} is the extinction coefficient, m_j is the complex refractive index and S_j is the scaling factor for the j-th aerosol component which represented the contribution of each aerosol component to the total columnar AOD. The S_j values were calculated by means of a least-square technique applied to the radiometric measurements over the spectral range minimizing the following quantity (Satheesh and Srinivasan, 2005):

$$\chi^2 = \sum_{i=1}^{N} \frac{\left(\tau_i^{mea} - \tau_i^{cal}\right)^2}{\left(\Delta\tau_i^{mea}\right)^2}, \quad (2)$$

where τ_i^{mea}, τ_i^{cal} are the measured and calculated AODs at the i-th wavelength, respectively; and $\Delta\tau_i^{mea}$ is the experimental error.

3. Results and discussion

3.1. Columnar aerosol optical and microphysical properties

Continuous observations were made with sun photometers at three sites (Fig. 1) during March 2012, and daily averages of AOD at 500 nm, $AE_{440-870\ nm}$, and WV were calculated (Fig. 2). Error bars in that figure denoted the daily standard deviations and therefore were a measure of the diurnal variation for a given day. Note that several gaps appeared in the time-series of daily AOD, AE and WV; these were due to cloud contamination and instrument problems. As shown in Fig. 2, similar trends were found for three sites for both aerosol optical properties (AOD and AE) and WV, suggesting widespread air pollution over the region during the study period.

The AOD is defined as the integral of extinction coefficient from the earth's surface to top of atmosphere, and as such it is an indicator of the columnar aerosol loading. In contrast, the AE is a measure of the spectral dependence of AOD, and so it provides information on the sizes of the atmospheric particles that affect the AOD. A larger AE indicates a dominance of smaller particles while smaller AEs are found for larger particles. The average AOD and AE (arithmetic mean ± standard deviation) over the HX site for the whole month were 0.69 ± 0.50 and 1.04 ± 0.28 respectively, and these values were comparable with the ones made at the other two sites. The AODs exhibited high values (>1.0) on six days in March, but the corresponding AEs during those events varied substantially, ranging from 0.5 to ~1.5. This large variability in AE suggested the dominance of coarse mode aerosols (AE < 1) during some of the pollution episodes and fine mode pollution aerosols (AE > 1) in others (Eck et al., 2010).

The average WV was only 0.48 cm for all the three sites, presumably due to the temperate-continental monsoon climate in Tianjin. Moreover, the daily WV followed a consistent trend, with higher WV coinciding with higher AODs, and this may be related to the humidification of the aerosol during pollution events. Summary statistics for AOD, AE and columnar WV at three sites were presented in Table 1. We focused our data analyses on the last week (24 to 30) of March because continuous records were available at all of the sites at that time. Two pollution episodes were characterized by high AODs (AOD > 1.0) in that week; these occurred on 26 and 29 March, respectively, but the two events showed markedly different AEs. That is, on 26 March the AE exceeded 1.50 while on 29 March it was lower by almost half. This presented us with an opportunity to investigate the mechanism responsible for spring pollution events, and our approach was based on a combination of multisource data and various interpretive techniques.

The aerosol volume-size distribution $dV(r)/d\ln r$ (unit: $\mu m^3/\mu m^2$) is an important parameter that is useful for understanding the behavior of aerosols in the climate system. Daily average aerosol volume-size distributions over three sites from 24 to 30 March were presented in Fig. 3, and the two pollution episodes were marked in blue and red for the 26th and 29th, respectively. It was evident that the volume

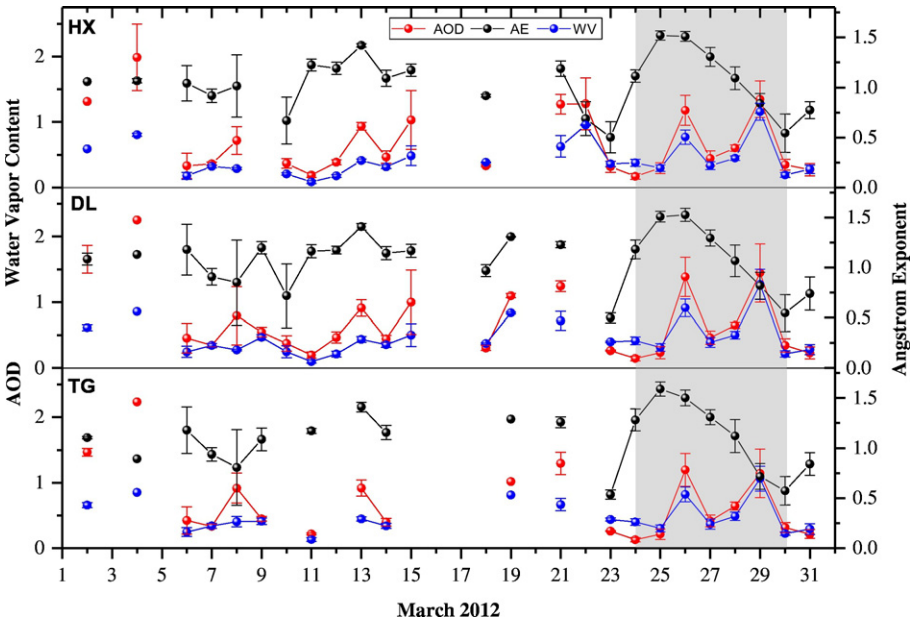

Fig. 2. Daily variation of aerosol optical depth (AOD) at 500 nm, Ångström Exponent (AE) for 440–870 nm and columnar water vapor content (WV, cm) in March 2012 retrieved from sunphotometer measurements over HX, DL and TG sites.

Table 1
Summary of statistics for aerosol optical depth (AOD), Ångström Exponent (AE), and columnar water vapor (WV) at three sites in Tianjin, March 2012.

Sites	Parameters	Mean ± SD[a]	Minimum	Maximum	N[b]
Hexi (HX)	AOD, unitless	0.69 ± 0.50	0.17	1.99	23
	AE, unitless	1.04 ± 0.28	0.50	1.52	
	WV, cm	0.48 ± 0.29	0.09	1.26	
Dongli (DL)	AOD	0.72 ± 0.55	0.15	2.25	24
	AE	1.08 ± 0.27	0.50	1.53	
	WV	0.47 ± 0.27	0.10	1.27	
Tanggu (TG)	AOD	0.71 ± 0.55	0.13	2.23	20
	AE	1.09 ± 0.29	0.54	1.59	
	WV	0.48 ± 0.25	0.13	1.06	

[a] SD stands for standard deviation.
[b] N stands for the number of the days with no less than three available measurements.

concentrations in fine mode were higher on 26 March than coarse mode for the HX and DL sites, but in contrast, higher volume concentrations were found in the coarse mode on 29 March. For the TG site, the aerosol volume concentration in coarse mode was considerably higher on 29 March despite the relatively similar fine mode aerosol volume concentrations on the two days. The ratios of volume fraction in fine mode (V_f) to the coarse mode (V_c) on 26 March at HX, DL and TG sites were 1.05, 1.16 and 0.66, respectively, while on 29 March, the ratios decreased to 0.19, 0.41 and 0.22, suggesting an increase in the particle size of the aerosol populations. This trend was consistent with the decrease in AE which fell from ~1.5 on 26 March to ~0.5 on 29 March (Fig. 2).

In addition to the AOD, AE and aerosol volume distributions, we analyzed the spectral SSA as part of our investigation into the variation in aerosol components during the two pollution episodes (Fig. 4). Defined as the ratio of scattering to total aerosol extinction, the SSA spectrum is sensitive not only to the variance in aerosol size but also to changes in aerosol type (Dubovik et al., 2002). The spectral SSA wavelength dependencies generally vary for different aerosol mixtures, and this can help distinguish among absorbing aerosol components (Wang et al., 2013b). As shown in Fig. 4, SSA generally decreased with wavelength for the range from 440 to 1020 nm at three sites except on 26 and 29 March. In this regard, Bond and Bergstrom (2006) showed that it's the case when BC was the dominant absorber. During pollution episodes, the spectral variations in SSA were markedly different relative to the clear conditions, and these differences were seen not only between the two cases but also among the three sites.

On 26 March (blue line in Fig. 4), the SSA increased with wavelength from 440 to 670 nm and decreased slightly from 670 to 1020 nm at both HX and DL sites; this was indication that brown carbon aerosols were present (Wang et al., 2013b). In contrast, the SSA for TG site presented a similar trend on 26 March with less polluted days. On 29 March (red line in Fig. 4), the SSA at three sites also followed an increasing pattern from 440 to 670 nm but unlike the earlier event, it continued to increase or stabilized between 670 and 870 nm. As demonstrated in Wang et al. (2013b), this type of SSA spectra pattern was an indication that mineral dust dominated the aerosols population.

Overall, based on the analyses of aerosol optical and microphysical properties, we can conclude that two episodes with high AODs occurred during the last week of March 2012. The sharp decrease in AE between events and the clear increase of the volume concentration in the coarse mode both indicated the dominance of anthropogenic particles in the fine mode on 26 March versus coarse mode particles (such as natural dust) on 29 March. Additionally, the major contributors to the enhanced absorption at blue wavelengths were found to be markedly different for the two events. For the pollution event on 26 March, the presence of brown carbon was revealed by the spectral variation of SSA. For the later event on 29 March, dust particles showed its predominance in aerosol absorption (at blue wavelength). For other days when the aerosol loading were not so high, BC was most likely the dominant absorber.

3.2. $PM_{2.5}$ chemical compositions

Along with radiometric measurements, $PM_{2.5}$ samples were simultaneously collected for chemical analyses during the daytime at each of the sites during the last week of March 2012. To understand the variations in $PM_{2.5}$ chemical compositions during the high PM episodes, we defined three types of cases based on the AOD and AE values as follows. On 26 March, high values were found for both AOD (>1.0) and AE (~1.5), and that event was identified as "haze" case. In contrast, the 29 March was considered as "dust" case due to the high value for AOD (>1.0) and low values for AE (~0.5). The AODs on 24 and 25 March were <0.3, and these were identified as "clear" cases.

The mass concentrations of water soluble ions, carbonaceous components, and elements at three sites for the three cases were presented in Fig. 5. In general, all three sites showed comparable concentrations and similar variability for the water-soluble ions and carbonaceous components during the three types of cases (top panels in Fig. 5). Compared with the clear case, both water-soluble ions and carbonaceous species exhibited substantially higher concentrations in the haze and dust cases, especially the former. For example, the concentrations of water-soluble ions on the hazy days were 5–19 times higher compared with those on the clear days, and the concentrations during dusty days were elevated over the clear conditions but this difference was lower than the hazy conditions, <8-fold. The lower concentrations of NO_3^-, SO_4^{2-} and NH_4^+ during dusty days compared with the hazy days may be related to the dilution effect of dust storms on these secondary species (Zhao et al., 2007; Huang et al., 2010).

The concentrations of major ions followed the order of $NO_3^- > SO_4^{2-} > NH_4^+ > Cl^- > K^+$ at all of the sites. The higher concentration of nitrates relative to sulfate probably resulted, at least in part, from the

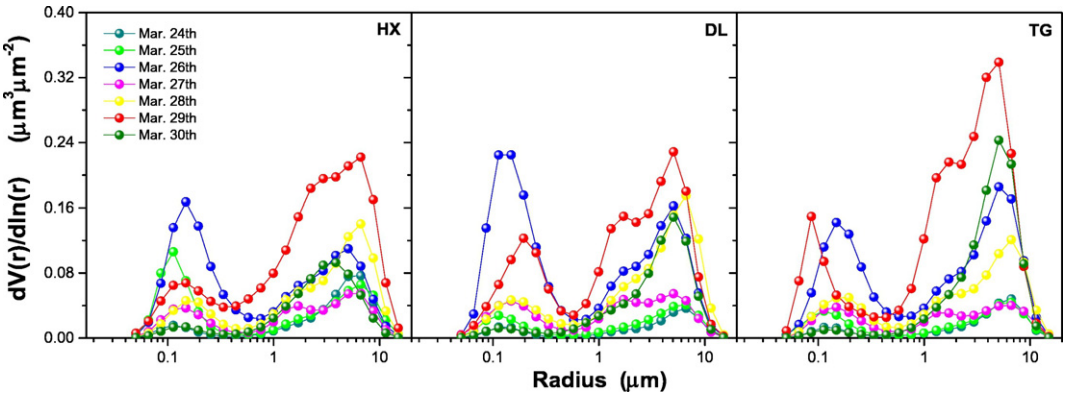

Fig. 3. Daily variation in aerosol volume-size distributions at three sites from 24 to 30 March 2012.

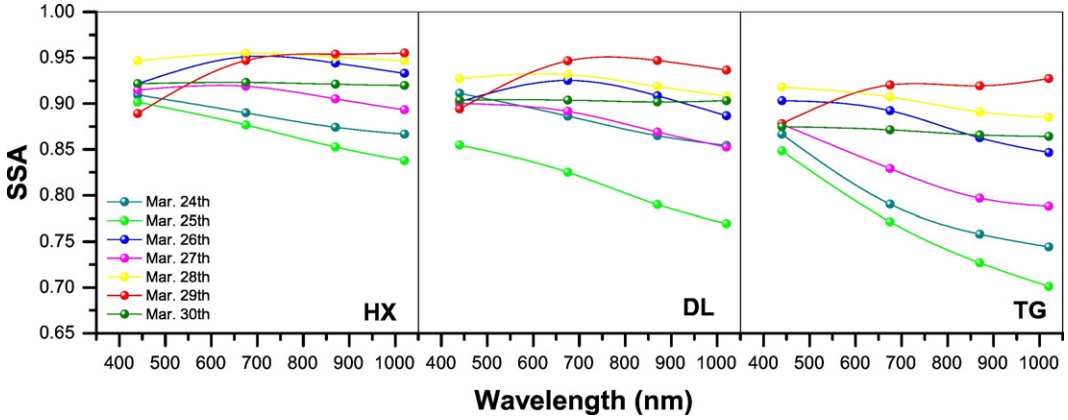

Fig. 4. Spectral variation in single scattering albedo (SSA) at three sites from 24 to 30 March 2012.

comparatively rapid heterogeneous formation of nitrate (approximately 10 times faster than sulfate, Hewitt, 2001). Carbonaceous species also showed increases during the haze and dust events, but there were not so pronounced as for the water-soluble ions (~3–4 times higher than on clear days). Higher concentrations of both OC and EC were found on the hazy day compared with the dusty day, and this can be explained by the fact that most of the OC and EC were emitted from pollution sources, especially fossil fuel combustion, biomass burning, vehicular exhaust and cooking (Zhao et al., 2013c).

With reference to the elements analyses (bottom panels in Fig. 5), we separated eight elements into three groups based on the results of enrichment factor (EF) analysis in a study by Huang et al. (2010). The first group included Al, Ca, Fe, Mg and Si; these are typically associated with mineral matter from the earth's crust. The second group consisted of Zn and Pb, which were moderately enriched and likely from both crustal and pollution sources. The last element, S, had EFs larger than 100, and it was classed as pollution element. As shown in Fig. 5, the elemental concentrations differed to varying degree during the haze and dust cases. Moreover, the concentrations of S, Zn and Pb were higher on the haze day than the dusty day at all the sites, while the crustal elements exhibited an opposite trends, except at the DL site where high emissions of metallic elements from iron and steel industries probably affected the elements that were typically classified as both crustal and pollution-derived.

3.3. Different causes for the two pollution episodes

3.3.1. Overview of two particle pollution episodes

The following analyses combined multi-scale observations with modeling techniques and also used meteorological data to highlight

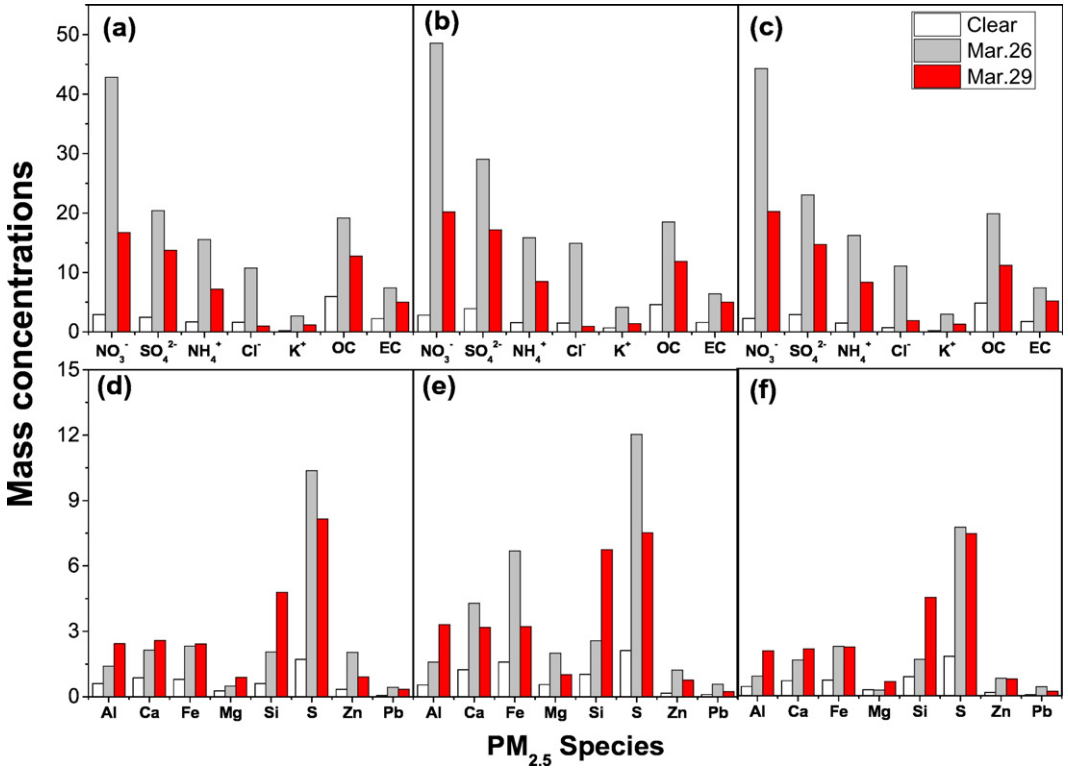

Fig. 5. Mass concentrations (μg m^{-3}) of major water-soluble ions and carbonaceous components (top panels) and selected elements (bottom panels) in $PM_{2.5}$ at three sites during clear, hazy, and dusty days.

possible causes for the two high PM episodes. The major $PM_{2.5}$ chemical species for the 26 and 29 March events were presented along with the corresponding aerosol optical properties results as group-contrast diagrams in Fig. 6. The methods used for the calculation of FAOD, FMF and AAOD were given in the Section 2.2.1 above.

As shown in Fig.6, unlike the carbonaceous components and secondary inorganic species (such as nitrate, sulfate and ammonium), soil dust increased to varying degrees over all the sites on 29 March compared with 26 March. This feature coincided with the lower AE, FAOD and FMF for the later event. Furthermore, the cumulative concentration of major contributors to aerosol extinction, that is, the sum of the secondary inorganic species, carbonaceous components and soil dust (Cao et al., 2012a), decreased by ~30% from the first event to the second, but the total AODs were similar. This may have resulted from the humidification of aerosols at HX and DL sites where the water vapor was higher during the second event (Fig. 6). A layer or layers of dust above the earth's surface probably also contributed to the columnar AODs, but these would not have been detectable through our surface-level chemical sampling. As regards the variation in aerosol absorption, both the lower SSA and the higher AAOD on 29 March compared with the haze event indicated that an increasing contribution of absorbing aerosols during the dust episodes at HX and TG sites.

3.3.2. Multi-scale observations, model estimations, and meteorological fields

Diurnal variations of ground-based aerosol optical properties along with the satellite observations, model simulation results, and synoptic maps were shown in Fig. 7 for both 26 and 29 March (left panels, a–c and right panels, d–f, respectively). The aerosol optical properties exhibited similar trends at the three sites, and therefore, only the results for AOD, AE and WV at the HX site were shown. On 26 March, AOD showed a decreasing trend from 1.86 at ~9:17 (local time) to 0.88 at ~14:47 and then the AOD increased slightly up to 1.07 at ~16:16 (Fig. 7a). Columnar water vapor content followed a trend similar to that of AOD. Variations in AE were not pronounced but maintained a high value of ~1.50; this implied high loading of anthropogenic fine PM on that day.

The contribution of regional transport during the first pollution episode was evaluated by examining the variability in the spatial distribution of MODIS/Terra AOD (Fig. 7b) along with the corresponding wind vectors at 850 hPa from ECMWF reanalysis dataset. On 25 March, most of the high AOD values appeared in eastern, central, and southern China while AODs over northern China, such as Tianjin, was quite low. Driven by southwesterly winds, the heavy aerosol loadings were transported to north China on 26 March, and that resulted in a wide swath of high AOD that spread over northern and eastern China. The

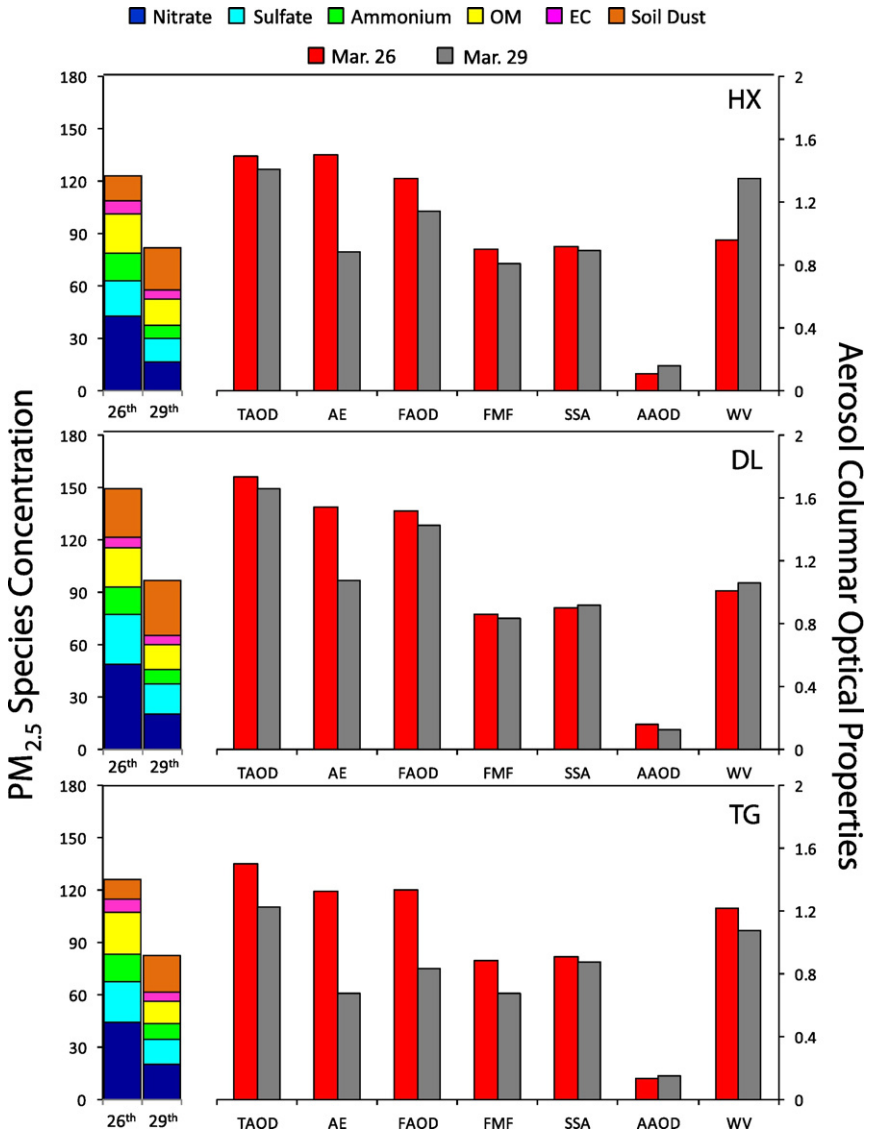

Fig. 6. General descriptions of $PM_{2.5}$ species (stacked columns in the left panels) and aerosol optical properties (grouped columns in the right panels) on 26 and 29 March 2012.

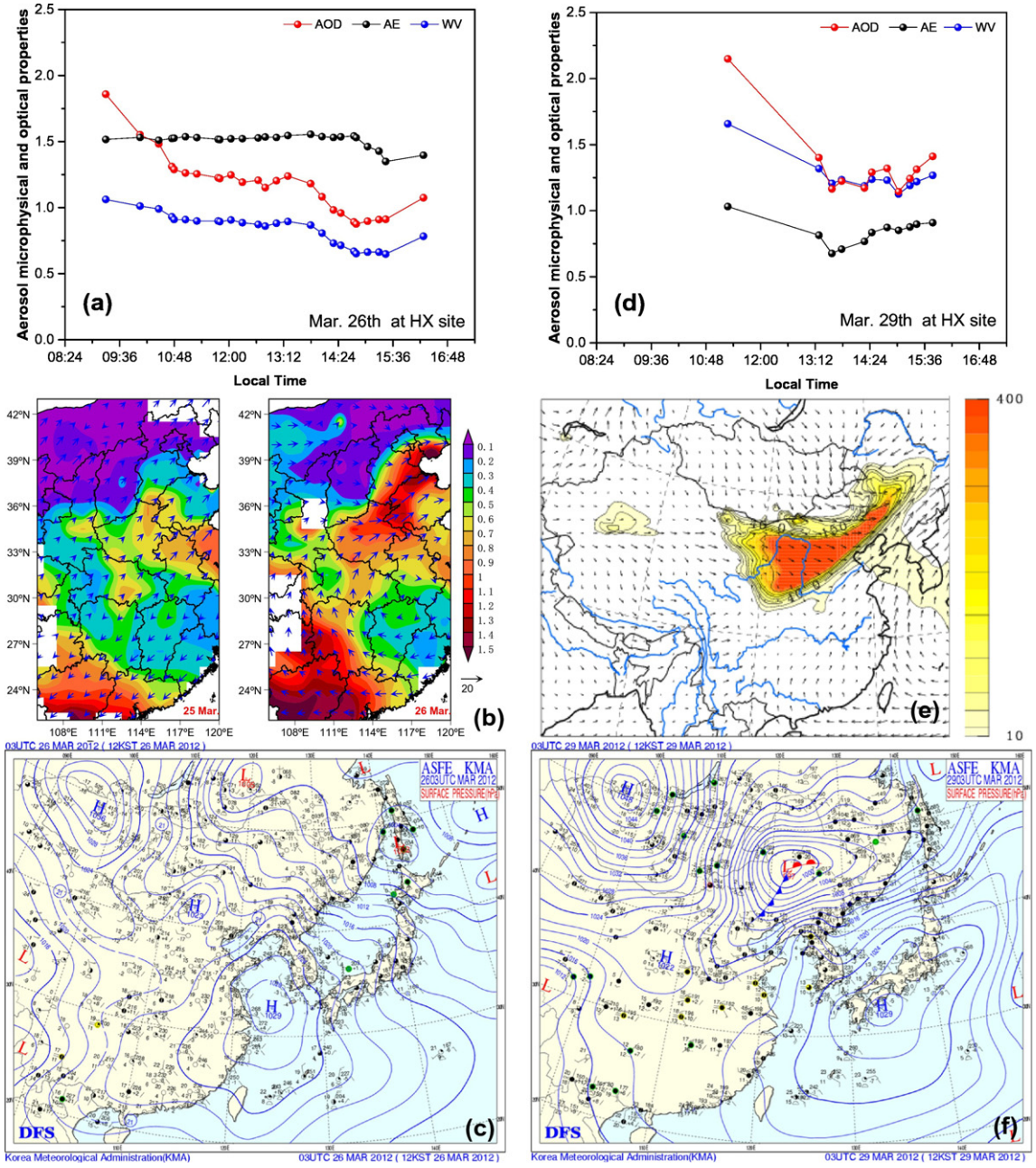

Fig. 7. Diurnal variation of ground-based aerosol optical properties along with the matching satellite observations, wind vectors, model simulations results, and synoptic maps on 26 (left panels, a–c) and 29 March (right panels, d–f), 2012. (a, d) Diurnal variation of AOD, AE, WV and temperatures; (b) MODIS AOD along with ECMWF wind fields at 850 hPa on 25 and 26 March; (e) dust concentrations simulated by RIAM-CFORS; (c, f) KMA synoptic maps (see text for abbreviations).

area with high AODs over Southern China approached and nearly merged with the plume in the northeast, and so aerosol pollutants were probably transported to our study sites from southwest. Moreover, a stagnant high-pressure system (generally associated with weak subsidence and light winds) over the Tianjin area (Fig. 7c) likely promoted the accumulation of air pollutants from both local emission and regional transport, and this, too, probably contributed to severity of the pollution episodes on 26 March.

Similar analyses were performed for the 29 March dust event (Fig. 7d–f) except that model simulations were used instead of satellite observations because no MODIS AOD retrievals were available on that day due to cloud contamination. As shown in Fig. 7d, AOD showed its maximum of 2.15 at ~11:16 and then rapidly decreased to 1.40 at ~13:16, followed by minor fluctuation, both AE and WV exhibited the similar trends with AOD. Nevertheless, AE always showed lower values by roughly half compared with those during the haze event, and this suggested an increase in the aerosol size during the dust event. The concentration of dust (in μg m^{-3}) estimated by RIAM-CFORS model (Fig. 7e) indicated that tons of dust particles were transported to Tianjin from sources region in northwest China. The possibility for long-range dust transport would also have been favored by the presence of a cold front (Fig. 7f) because these conditions are generally associated with dust storm (Tao et al., 2006).

Vertical retrievals from space-borne Lidar CALIOP aboard CALIPSO satellite were also used in this study to complement the ground-based measurements. Designed to acquire the vertical structure of aerosols and clouds, CALIPSO has showed unique advantages for evaluating regional transport in air pollution monitoring (Huang et al., 2008; Qin et al., 2016). Three types of CALIOP images were considered in this section; these included the total attenuated backscatter coefficient (TABC, Fig. 8a,

d), the volume depolarization ratio (VDR, Fig. 8b, e) at 532 nm, and vertical feature masks (VFM, Fig. 8c, f). These data were obtained from the CALIPSO website (http://www-calipso.larc.nasa.gov/).

The rectangular boxes shown in each frame in Fig. 8 showed the sampling sites and their surrounding areas along with the satellite swaths that covered the study region (Fig. 8a, d). Note that the CALIOP detection at ~02:30 (night time) was used for the 29 March event because the daytime images were unavailable. Dust concentrations estimated by the RIAM-CFORS model at the time closest to the satellite overpass were also presented as an inset (Fig. 8e). Thick external aerosol layers were observed on both 26 and 29 March (Fig. 8a and d), passing over Tianjin and mixing downward into the local aerosol emissions. The height of the aerosol layer on 26 March was ~5 km while the thick aerosol layer on 29 March extended up to ~10 km. These features were consistent with the information obtained from the VFM images (Fig. 8c, f); in addition, the external aerosol layers with high VDR values on 29 March can be conditionally identified as dust aerosols because they were typically nonspherical (Huang et al., 2008).

To further characterize the two pollution episodes, the contribution of different aerosol species was quantified using the technique described in Section 2.3. Fractional AODs for five species were calculated and the results were presented in Fig. 9. Note that the contributions from SS and MD covered all the modes of the corresponding species. Water-soluble species dominate the total AOD on the hazy day (contributing ~70% on 26 March, Fig. 9) while both insoluble components and mineral dust made significant contribution on 29 March (~18% and ~13% respectively). According to the description in Hess et al. (1998), insoluble species also included soil particles, and that can cause an underestimation of MD AOD fraction. The contribution of BC to the total AOD showed relatively small differences between two events. Additionally, sea-salt particles showed negligible contributions to the columnar AODs even though the sampling site was in a coastal region.

4. Conclusions

Simultaneous measurements of columnar aerosol microphysical and optical properties as well as $PM_{2.5}$ chemical compositions were made at Tianjin, a coastal megacity in China to investigate springtime pollution events. Two types of episodes were observed during the last week of March 2012 based on aerosol optical properties and $PM_{2.5}$ chemical compositions. During the first event, which appeared on 26 March, the daily average AOD was ~1.18 and ranged from 0.88 to 1.86, while AE varied from 1.35 to 1.55 and showed a daily average > 1.50. By contrast, the mean AOD on 29 March event was 1.35 ± 0.28, showing the maximum of 2.15, and the AE (0.84) was much lower than during the earlier event. The high AODs combined with different AEs implied different sizes of the dominant aerosols during these two pollution episodes, and this was confirmed by measurements of volume-size distributions. Moreover, the SSA spectra indicated that brown carbon and dust were the major contributors to the enhanced absorption at blue wavelengths

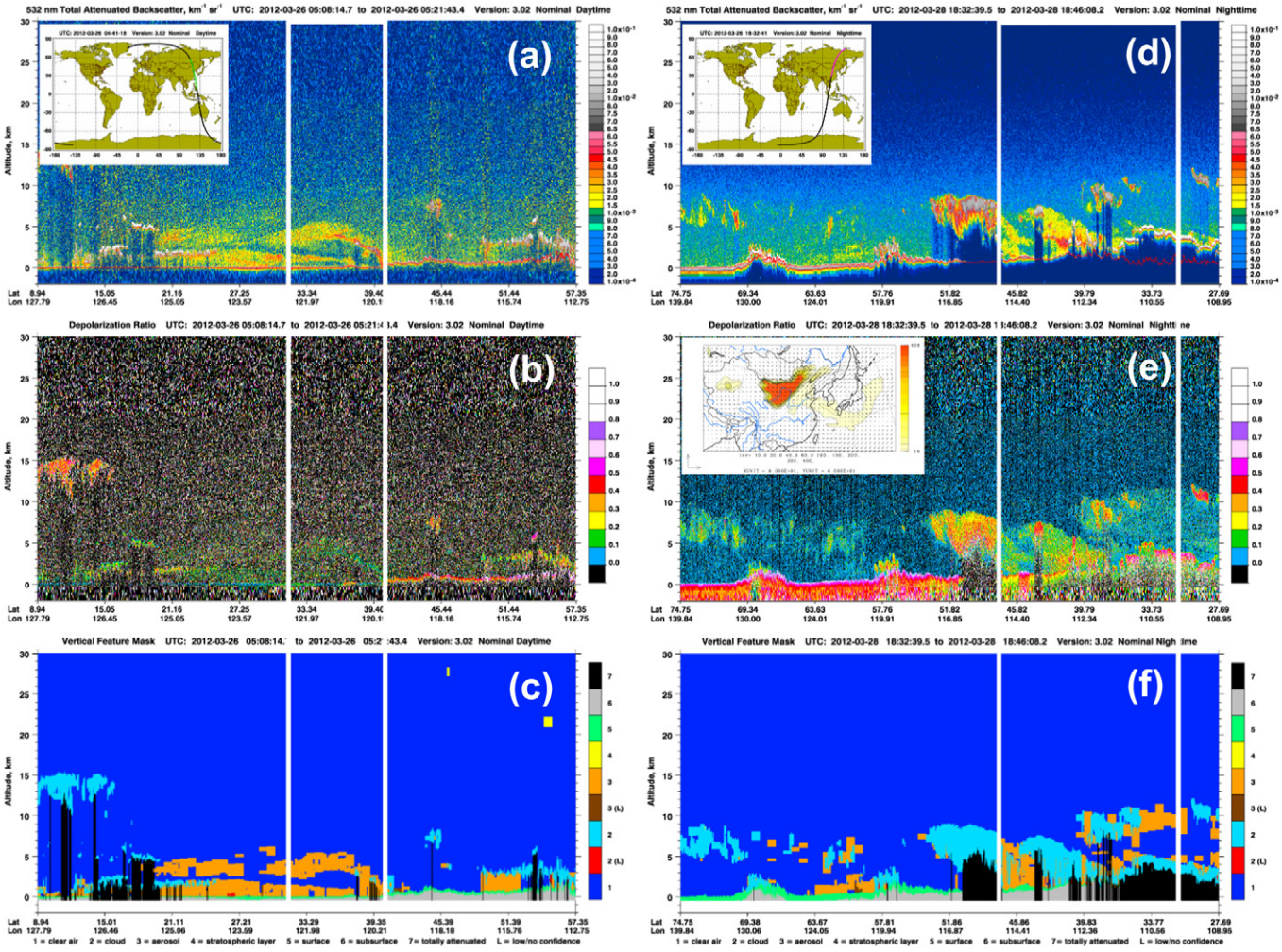

Fig. 8. Time-height cross-section of CALIPSO products during pollution episodes on 26 March (left panels, a–c) and 29 March 2012 (right panels, d–f). The rectangular boxes in the panels showed the presence of aerosol transport layer over the study region. (a, d) Total attenuated backscatter at 532 nm; (b, e) depolarization ratio; and (c, f) vertical feature mask. Also shown in the insets were (a, d) the satellite orbital tracks around Tianjin and (e) and the dust concentration simulated by RIAM-CFORS.

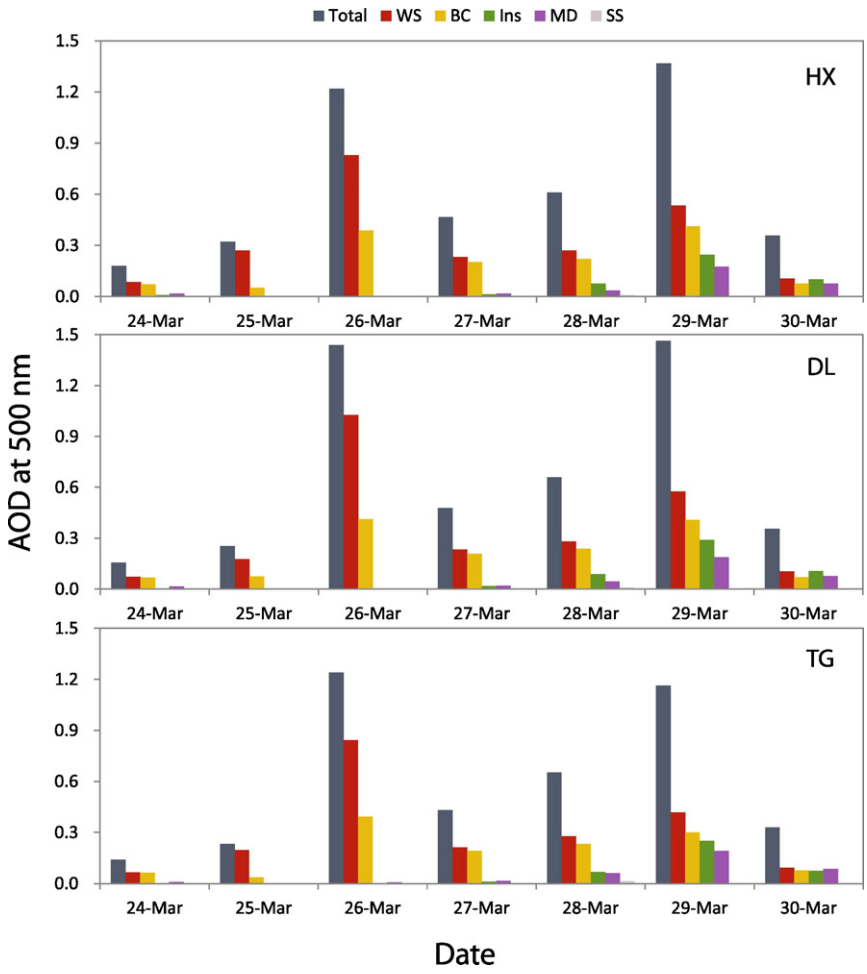

Fig. 9. Contributions of selected aerosol species to the columnar AOD estimated by the technique developed in this study (see text for details).

on 26 and 29 March, respectively. Compared with clear conditions, both of the pollution events showed increases to varying degrees in concentrations of water-soluble ions, carbonaceous components, and selected elements. Generally, the increases in water-soluble ions and carbonaceous components were greater for the earlier event than the later one. For the elements, however, only the pollution elements followed the same pattern, and the crustal elements from desert dust were higher in the second event.

Satellite observations were combined with model simulations and analyses of meteorological fields to investigate the causes of these two particulate pollution episodes. The 26 March event was attributed to the accumulation of local pollution emissions combined with substances transported from the southwest of Tianjin due to the presence of a high-pressure system. By contrast, the high aerosol loading on 29 March probably resulted from the mixing of local urban pollution with dust transported long distances from source regions northwest. The two different types of pollution episodes that occurred in one week demonstrated the complexity of processes responsible for high aerosol loading over this region and the rapidity with which conditions change. The combination of multi-scale observations showed an excellent potential for investigating the causes for particle pollution. The results of this study have improved our knowledge on the causes for spring particle pollution over Tianjin and they should also aid in framing regional air-quality management policies.

Acknowledgments

This work was supported by the National Basic Research Program (Grant No. 2010CB950801), the project from "Strategic Priority Research Program" of the Chinese Academy of Sciences (Grant No. XDB05060500) and the National Natural Science Foundation of China (Grant No. 41505032). Dr. Calvello was partially supported by the CNR (Italy) under STM-2015 grant. We also extended our gratitude to the Sun/sky-radiometer Observation Network (SONET), CALIPSO, MODIS, RIAM-CFORS and ECMWF team for the dataset used in our work.

References

Bi, X., Feng, Y., Wu, J., Wang, Y., Zhu, T., 2007. Source apportionment of PM10 in six cities of northern China. Atmos. Environ. 41, 903–912.
Bond, T.C., Bergstrom, R.W., 2006. Light absorption by carbonaceous particles: an investigative review. Aerosol Sci. Technol. 40, 27–67.
Cao, J.J., Lee, S.C., Ho, K.F., Zhang, X.Y., Zou, S.C., Fung, K., Watson, J.G., Chow, J.C., 2003. Characteristics of carbonaceous aerosol in Pearl River Delta region, China during 2001 winter period. Atmos. Environ. 37, 1451–1460.
Cao, J.J., Wang, Q.Y., Chow, J.C., Watson, J.G., Tie, X.X., Shen, Z.X., Wang, P., An, Z.S., 2012a. Impacts of aerosol compositions on visibility impairment in Xi'an, China. Atmos. Environ. 59, 559–566.
Cao, J.J., Xu, H.M., Xu, Q., Chen, B.H., Kan, H.D., 2012b. Fine particulate matter constituents and cardiopulmonary mortality in a heavily polluted Chinese city. Environ. Health Perspect. 120 (3), 373–378.
Chen, Y., Xie, S.D., 2014. Spatiotemporal pattern and regional characteristics of visibility in China during 1976–2010. Chin. Sci. Bull. 3054–3065.
Chow, J.C., Watson, J.G., 2002. $PM_{2.5}$ carbonate concentrations at regionally 28 representative interagency monitoring of protected visual environment sites. J. Geophys. Res. 107 (D21). http://dx.doi.org/10.1029/2001JD000574.
Chu, D.A., Kaufman, Y.J., Zibordi, G., Chern, J.D., Mao, J., Li, C., Holben, B.N., 2003. Global monitoring of air pollution over land from the Earth Observing System-Terra moderate resolution imaging spectroradiometer (MODIS). J. Geophys. Res. 108 (D21):4661. http://dx.doi.org/10.1029/2002JD003179.
Dubovik, O., King, M.D., 2000. A flexible inversion algorithm for retrieval of aerosol optical properties from sun and sky radiance measurements. J. Geophys. Res. 105, 673–696.
Dubovik, O., Smirnov, A., Holben, B.N., King, M.D., Kaufman, Y.J., Eck, T.F., Slutsker, I., 2000. Accuracy assessments of aerosol optical properties retrieved from Aerosol Robotic

Network (AERONET) sun and sky radiance measurements. J. Geophys. Res. 105, 9791–9806.
Dubovik, O., Holben, B., Thmoas, F.E., 2002. Variability of absorption and optical properties of key aerosol types observed in worldwide locations. J. Atmos. Sci. 59 (3), 590–608.
Dubovik, O., Sinyuk, A., Lapyonok, T., Holben, B.N., Mishchenko, N., Yang, P., Eck, T.F., Volten, H., Munoz, O., Veihelmann, B., Zander, V.D., Sorokin, M., Slutsker, I., 2006. Application of light scattering by spheroids for accounting for particle nonsphericity in remote sensing of desert dust. J. Geophys. Res. 111. http://dx.doi.org/10.1029/2005JD006619.
Eck, T.F., Holben, B.N., Sinyuk, A., Pinker, R.T., Goloub, P., Chen, H., et al., 2010. Climatological aspects of the optical properties of fine/coarse mode aerosol mixtures. J. Geophys. Res. 115. http://dx.doi.org/10.1029/2010JD014002.
Fenger, J., 2009. Air pollution in the last 50 years – from local to global. Atmos. Environ. 43, 13–22.
Guo, S., Hu, M., Zamora, M.L., Peng, J.F., Shang, D.J., Zheng, J., Du, Z.F., Wu, Z.J., Shao, M., Zeng, L.M., Molina, M.J., Zhang, R.Y., 2014. Elucidating severe urban haze formation in China. PNAS 111 (49):17373–17378. http://dx.doi.org/10.1073/pnas.1419604111.
He, X., Li, C.C., Lau, A.K.H., Deng, Z.Z., Mao, J.T., Wang, M.H., Liu, X.Y., 2009. An intensive study of aerosol optical properties in Beijing urban area. Atmos. Chem. Phys. 9: 8903–8915. http://dx.doi.org/10.5194/acp-9-8903-2009.
Hess, M., Koepke, P., Schult, I., 1998. Optical properties of aerosols and clouds: the software package OPAC. Bull. Am. Meteorol. Soc. 79, 831–844.
Hewitt, C.N., 2001. The atmospheric chemistry of sulfur and nitrogen in power station plumes. Atmos. Environ. 35, 1155–1170.
Holben, B.N., Eck, T.F., Slutsker, I., Tanré, D., Buis, J.P., Setzer, A., Vermote, E., Reagan, J.A., Kaufman, Y.J., Nakajima, T., Lavenu, F., Jankowiak, I., Smirnov, A., 1998. AERONET - a federated instrument network and data archive for aerosol characterization. Remote Sens. Environ. 66, 1–16.
Hu, M., Guo, S., Peng, J.F., Wu, Z.J., 2015. Insight into characteristics and sources of $PM_{2.5}$ in the Beijing-Tianjin-Hebei region, China. Natl. Sci. Rev. 2 (3), 257–258.
Huang, J., Minnis, P., Chen, B., Huang, Z., Liu, Z., Zhao, Q., Yi, Y., Ayers, J.K., 2008. Long-range transport and vertical structure of Asian dust from CALIPSO and surface measurements during PACDEX. J. Geophys. Res. 113. http://dx.doi.org/10.1029/2008JD010620.
Huang, K., Zhuang, G., Li, J., Wang, Q., Sun, Y., Lin, Y., Fu, J.S., 2010. Mixing of Asian dust with pollution aerosol and the transformation of aerosol components during the dust storm over China in spring 2007. J. Geophys. Res. 115. http://dx.doi.org/10.1029/2009JD013145.
Huang, R.J., Zhang, Y.L., Bozzetti, C., Ho, K.F., Cao, J.J., Han, Y.M., et al., 2014. High secondary aerosol contribution to particulate pollution during haze events in China. Nature 514, 218–222.
Ji, D.S., Wang, Y.S., Wang, L.L., Chen, L.F., Hu, B., Tang, G.Q., Xin, J.Y., Song, T., Wen, T.X., Sun, Y., Pan, Y.P., Liu, Z.R., 2012. Analysis of heavy pollution episodes in selected cities of northern China. Atmos. Environ. 50, 338–348.
Kaufman, Y.J., Tanré, D., Boucher, O., 2002. A satellite view of aerosols in the climate system. Nature 419, 215–223.
King, M.D., Kaufman, Y.J., Menzel, W.P., Tanre, D., 1992. Remote sensing of cloud, aerosol, and water vapor properties from the moderate resolution imaging spectrometer (MODIS). IEEE Trans. Geosci. Remote 30 (1), 2–27.
Kong, S.F., Han, B., Bai, Z.P., Chen, L., Shi, J.W., Xu, Z., 2010. Receptor modeling of $PM_{2.5}$, PM_{10} and TSP in different seasons and long-range transport analysis at a coastal site of Tianjin, China. Sci. Total Environ. 408, 4681–4694.
Levy, R.C., Mattoo, S., Munchak, L.A., Remer, L.A., Sayer, A.M., Patadia, F., Hsu, N.C., 2013. The collection 6 MODIS aerosol products over land and ocean. Atmos. Meas. Tech. 6 (11), 2989–3034.
Li, Z., Blarel, L., Podvin, T., Goloub, P., Buis, J.P., Morel, J.P., 2008. Transferring the calibration of direct solar irradiance to diffuse sky radiance measurements for CIMEL sun-sky radiometers. Appl. Opt. 47, 1368–1377.
Li, Z., Goloub, P., Dubovik, O., Blarel, L., Zhang, W., Podvin, T., Sinyuk, A., Sorokin, M., Chen, H., Holben, B., Tanré, D., Canini, M., Buis, J.P., 2009. Improvements for ground-based remote sensing of atmospheric aerosol properties by additional polarimetric measurements. J. Quant. Spectrosc. Radiat. Transf. 110, 1954–1961.
Liu, X.G., Li, J., Qu, Y., Han, T., Hou, L., Gu, J., Chen, C., Yang, Y., Liu, X., Yang, T., Zhang, Y., Tian, H., Hu, M., 2013. Formation and evolution mechanism of regional haze: a case study in the megacity Beijing, China. Atmos. Chem. Phys. 13:4501–4514. http://dx.doi.org/10.5194/acp-13-4501-2013.
Mao, K.B., Ma, Y., Xia, L., Chen, W.Y., Shen, X.Y., He, T.J., Xu, T.R., 2014. Global aerosol change in the last decades: an analysis based on MODIS data. Atmos. Environ. 94, 680–686.
Miura, K., Furutani, H., Iwamoto, Y., Nagano, K., Kobayashi, H., Mochida, M., et al., 2014. New Particle Formation of Marine Aerosols. Western Pacific Air-Sea Interaction Study.
Omar, A.H., Winker, D.M., Kittaka, C., Vaughan, M.A., et al., 2009. The CALIPSO automated aerosol classification and lidar ratio selection algorithm. J. Atmos. Ocean. Technol. 26 (10), 1994–2014.
Pavese, G., Lettino, A., Calvello, M., Esposito, F., Fiore, S., 2015. Aerosol composition and properties variation at the ground and over the column under different air masses advection in South Italy. Environ. Sci. Pollut. Res. http://dx.doi.org/10.1007/s11356-015-5860-1.
Pöschl, U., 2005. Atmospheric aerosols: composition, transformation, climate and health effects. Angew. Chem. Int. Ed. 44:7520–7540. http://dx.doi.org/10.1002/anie.200501122.
Qin, K., Wu, L.X., Wong, M.S., Letu, H., Hu, M.Y., Lang, H.M., Sheng, S.J., Teng, J.Y., Xiao, X., Yuan, L.M., 2016. Trans-boundary aerosol transport during a winter haze episode in China revealed by ground-based Lidar and CALIPSO satellite. Atmos. Environ. 141, 20–29.
Quan, J., Zhang, Q., He, H., Liu, J., Huang, M., Jin, H., 2011. Analysis of the formation of fog and haze in North China Plain (NCP). Atmos. Chem. Phys. 11:8205–8214. http://dx.doi.org/10.5194/acp-11-8205-2011.
Satheesh, S.K., Srinivasan, J.A., 2005. Method to estimate aerosol radiative forcing from spectral optical depths. J. Atmos. Sci. 1082-1092, 63.
Shen, Z.X., Arimoto, R., Okuda, T., Cao, J.J., Zhang, R.J., Li, X.X., Du, N., Nakao, S., Tanaka, S., 2008. Seasonal variations and evidence for the effectiveness of pollution controls on water-soluble inorganic species in TSP and PM2.5 from Xi'an, China. J. Air Waste Manage. Assoc. 58, 1560–1570.
Smirnov, A., Holben, B.N., Eck, T.F., Dubovik, O., Slutsker, I., 2000. Cloud screening and quality control algorithms for the AERONET database. Remote Sens. Environ. 73, 337–349.
Tao, G., Xu, Y.F., Bo, Y.H., Yu, X., 2006. Synoptic characteristics of dust storms observed in Inner Mongolia and their influence on the downwind area (the Beijing-Tianjin region). Meteorol. Appl. 13, 393–403.
Tao, M.H., Chen, L.F., Xiong, X.Z., Zhang, M.G., Ma, P.F., Tao, J.H., Wang, Z.F., 2014. Formation process of the widespread extreme haze pollution over northern China in January 2013: implications for regional air quality and climate. Atmos. Environ. 98, 417–425.
Tie, X.X., Cao, J.J., 2009. Aerosol pollution in China: present and future impact on environment. Particuology 7, 426–431.
Tie, X.X., Huang, R.J., Dai, W.T., Cao, J.J., Long, X., Su, X.L., Zhao, S.Y., Wang, Q.Y., Li, G.H., 2016. Effect of heavy haze and aerosol pollution on rice and wheat productions in China. Sci. Rep. 6. http://dx.doi.org/10.1038/srep29612.
Uno, I., Carmichael, G.R., Streets, D.G., Tang, Y., Yienger, J.J., et al., 2003. Regional chemical weather forecasting system CFORS: model descriptions and analysis of surface observations at Japanese island stations during the ACE-Asia experiment. J. Geophys. Res. 108 (D23):8668. http://dx.doi.org/10.1029/2002JD002845.
Uno, I., Satake, S., Carmichael, G.R., Tang, Y., et al., 2004. Numerical study of Asian dust transport during the springtime of 2001 simulated with the Chemical Weather Forecasting System (CFORS) model. J. Geophys. Res. 109, D19S24. http://dx.doi.org/10.1029/2003JD004222.
Wang, Q., Cao, J., Tao, J., Li, N., Su, X., Chen, L.W.A., Wang, P., Shen, Z., Liu, S., Dai, W., 2013a. Long-term trends in visibility and at Chengdu, China. PLoS ONE 8, e68894. http://dx.doi.org/10.1371/journal.pone.0068894.
Wang, L., Li, Z., Tian, Q., Ma, Y., Zhang, F., Zhang, Y., Li, D., Li, K., Li, L., 2013b. Estimate of aerosol absorbing components of black carbon, brown carbon, and dust from ground-based remote sensing data of sun-sky radiometers. J. Geophys. Res. Atmos. 118:6534–6543. http://dx.doi.org/10.1002/jgrd.50356.
Wang, L.T., Wei, Z., Yang, J., Zhang, Y., Zhang, F.F., Su, J., Meng, C.C., Zhang, Q., 2014a. The 2013 severe haze over southern Hebei, China: model evaluation, source apportionment, and policy implications. Atmos. Chem. Phys. 14:3151–3173. http://dx.doi.org/10.5194/acp-14-3151-2014.
Wang, Y.S., Yao, L., Wang, L.L., et al., 2014b. Mechanism for the formation of the January 2013 heavy haze pollution episode over central and eastern China. Sci. China Earth Sci. 57:14–25. http://dx.doi.org/10.1007/s11430-013-4773-4.
Wang, Z.F., Li, J., Wang, Z., Yang, W.Y., Tang, X., Ge, B.Z., et al., 2014c. Modeling study of regional severe hazes over mid-eastern China in January 2013 and its implications on pollution prevention and control. Sci. China Earth Sci. 57:3–13. http://dx.doi.org/10.1007/s11430-013-4793-0.
Wang, L.L., Liu, Z.R., Sun, Y., Ji, D.S., Wang, Y.S., 2015. Long-range transport and regional sources of $PM_{2.5}$ in Beijing based on long-term observations from 2005 to 2010. Atmos. Res. 157, 37–48.
Wang, Q., Huang, R.J., Cao, J., Tie, X., Shen, Z., Zhao, S., Han, Y., Li, G., Li, Z., Ni, H., Zhou, Y., Wang, M., Chen, Y., Su, X., 2016. Contribution of regional transport to the black carbon aerosol during winter haze period in Beijing. Atmos. Environ. 132, 11–18.
Watson, J.G., Chow, J.C., Frazier, C.A., 1999. X-ray fluorescence analysis of ambient air samples. In: Landsberger, S., Creatchman, M. (Eds.), Elemental Analysis of Airborne Particles. Gordon and Breach Publishers, New York, NJ, pp. 67–96.
Xu, H.M., Cao, J.J., Ho, K.F., Ding, H., Han, Y.M., Wang, G.H., Chow, J.C., Watson, J.G., Khol, S.D., Qiang, J., Li, W.T., 2012. Lead concentrations in fine particulate matter after the phasing out of leaded gasoline in Xi'an, China. Atmos. Environ. 46, 217–224.
Yuan, H., Zhuang, G.S., Li, J., Wang, Z.F., Li, J., 2008. Mixing of mineral with pollution aerosols in dust season in Beijing: revealed by source apportionment study. Atmos. Environ. 42, 2141–2157.
Zhang, Y., Li, Z.Q., 2015. Remote sensing of atmospheric fine particulate matter ($PM_{2.5}$) mass concentration near the ground from satellite observation. Remote Sens. Environ. 160, 252–262.
Zhang, T., Cao, J.J., Tie, X.X., Shen, Z.X., Liu, S.X., Ding, H., Han, Y.M., Wang, G.H., Ho, K.F., Qiang, J., Li, W.T., 2011. Water-soluble ions in atmospheric aerosols measured in Xi'an, China: seasonal variations and sources. Atmos. Res. 201, 110–119.
Zhang, X.Y., Wang, Y.Q., Niu, T., Zhang, X.C., Gong, S.L., Zhang, Y.M., Sun, J.Y., 2012. Atmospheric aerosol compositions in China: spatial/temporal variability, chemical signature, regional haze distribution and comparisons with global aerosols. Atmos. Chem. Phys. 12:779–799. http://dx.doi.org/10.5194/acp-12-779-2012.
Zhang, R., Jing, J., Tao, J., Hsu, S.-C., Wang, G., Cao, J., Lee, C.S.L., Zhu, L., Chen, Z., Zhao, Y., Shen, Z., 2013. Chemical characterization and source apportionment of $PM_{2.5}$ in Beijing: seasonal perspective. Atmos. Chem. Phys. 13:7053–7074. http://dx.doi.org/10.5194/acp-13-7053-2013.
Zhang, R.Y., Li, Q., Zhang, R.N., 2014a. Meteorological conditions for the persistent severe fog and haze event over eastern China in January 2013. Sci. China Earth Sci. 57:26–35. http://dx.doi.org/10.1007/s11430-013-4774-3.
Zhang, J.K., Sun, Y., Liu, Z.R., Ji, D.S., Hu, B., Liu, Q., Wang, Y.S., 2014b. Characterization of submicron aerosols during a month of serious pollution in Beijing, 2013. Atmos. Chem. Phys. 14:2887–2903. http://dx.doi.org/10.5194/acp-14-2887-2014.
Zhang, T., Cao, J.J., Chow, J.C., Shen, Z.X., Ho, K.F., Ho, S.H., Liu, S.X., Han, Y.M., Watson, J.G., Wang, G.H., Huang, R.J., 2014c. Characterization and seasonal variations of

levoglucosan in fine particulate matter in Xi'an, China. J. Air Waste Manage. 64 (11): 1317–1327. http://dx.doi.org/10.1080/10962247.2014.944959.
Zhao, X.J., Zhuang, G.S., Wang, Z.F., Sun, Y.L., Wang, Y., Yuan, H., 2007. Variation of sources and mixing mechanism of mineral dust with pollution aerosol - revealed by the two peaks of a super dust storm in Beijing. Atmos. Res. 84, 265–279.
Zhao, P.S., Zhang, X.L., Xu, X.F., Zhao, X.J., 2011. Long-term visibility trends and characteristics in the region of Beijing, Tianjin, and Hebei, China. Atmos. Res. 101, 711–718.
Zhao, X.J., Zhao, P.S., Xu, J., Meng, W., Pu, W.W., Dong, F., He, D., Shi, Q.F., 2013a. Analysis of a winter regional haze event and its formation mechanism in the North China Plain. Atmos. Chem. Phys. 13:5685–5696. http://dx.doi.org/10.5194/acp-13-5685-2013.
Zhao, P.S., Dong, F., He, D., Zhao, X.J., Zhang, X.L., Zhang, W.Z., Yao, Q., Liu, H.Y., 2013b. Characteristics of concentrations and chemical compositions for $PM_{2.5}$ in the region of Beijing, Tianjin, and Hebei, China. Atmos. Chem. Phys. 13:4631–4644. http://dx.doi.org/10.5194/acp-13-4631-2013.
Zhao, P.S., Dong, F., Yang, Y.D., He, D., Zhao, X.J., Zhang, W.Z., Yao, Q., Liu, H.Y., 2013c. Characteristics of carbonaceous aerosol in the region of Beijing, Tianjin, and Hebei, China. Atmos. Environ. 71, 389–398.